



UNIVERSITY OF LEEDS

This is a repository copy of *Ultra-low-threshold continuous-wave and pulsed lasing in tensile-strained GeSn alloys*.

White Rose Research Online URL for this paper:
<http://eprints.whiterose.ac.uk/157738/>

Version: Accepted Version

Article:

Elbaz, A, Buca, D, von den Driesch, N et al. (15 more authors) (2020) Ultra-low-threshold continuous-wave and pulsed lasing in tensile-strained GeSn alloys. *Nature Photonics*, 14 (6). pp. 375-382. ISSN 1749-4885

<https://doi.org/10.1038/s41566-020-0601-5>

© The Author(s), under exclusive licence to Springer Nature Limited 2020. This is an author produced version of a journal article published in *Nature Photonics*. Uploaded in accordance with the publisher's self-archiving policy.

Reuse

Items deposited in White Rose Research Online are protected by copyright, with all rights reserved unless indicated otherwise. They may be downloaded and/or printed for private study, or other acts as permitted by national copyright laws. The publisher or other rights holders may allow further reproduction and re-use of the full text version. This is indicated by the licence information on the White Rose Research Online record for the item.

Takedown

If you consider content in White Rose Research Online to be in breach of UK law, please notify us by emailing eprints@whiterose.ac.uk including the URL of the record and the reason for the withdrawal request.



eprints@whiterose.ac.uk
<https://eprints.whiterose.ac.uk/>

Ultra-low threshold continuous-wave and pulsed lasing in tensile strained GeSn alloys

Anas Elbaz^{1,2}, Dan Buca^{3,*}, Nils von den Driesch^{3,4}, Konstantinos Pantzas¹, Gilles Patriarche¹, Nicolas Zerounian¹, Etienne Herth¹, Xavier Checoury¹, Sébastien Sauvage¹, Isabelle Sagnes¹, Antonino Foti⁵, Razvigor Ossikovski⁵, Jean-Michel Hartmann⁶, Frédéric Boeuf², Zoran Ikonc⁷, Philippe Boucaud⁸, Detlev Grützmacher^{3,4}, and Moustafa El Kurdi^{1,*}

¹Center for Nanoscience and Nanotechnology, C2N UMR 9001, CNRS, Université Paris Sud, Université Paris Saclay, 91120 Palaiseau, France

²STMicroelectronics, Rue Jean Monnet 38054 Crolles, France

³Peter Grünberg Institute (PGI 9) and JARA-Fundamentals of Future Information Technologies, Forschungszentrum Juelich, 52428 Juelich, Germany

⁴JARA-Institute Green IT, RWTH Aachen, 52062 Aachen, Germany

⁵LPICM, CNRS, Ecole Polytechnique, Université Paris-Saclay, 91128 Palaiseau, France

⁶CEA, LETI and Univ. Grenoble Alpes, 38054 Grenoble, France

⁷Pollard Institute, School of Electronic and Electrical Engineering, University of Leeds, Leeds LS2 9JT, UK

⁸Université Côte d'Azur, CNRS, CRHEA, 06560 Valbonne, France

*corresponding authors: moustafa.el-kurdi@u-psud.fr, d.m.buca@fz-juelich.de

ABSTRACT

Strained GeSn alloys are promising for realizing light emitters based entirely on group IV elements. Here, we report GeSn microdisk lasers encapsulated with a SiNx stressor layer to produce tensile strain. A 300nm GeSn layer with 5.4 at. % Sn, which is an indirect band-gap semiconductor as-grown, is transformed via tensile strain engineering into a direct band-gap semiconductor that supports lasing. In this approach the low Sn concentration enables improved defect engineering and the tensile strain delivers a low density of states at the valence band edge, which is the light hole band. We observe ultralow-threshold continuous wave (cw) and pulsed lasing at temperatures of up to 70K and 100K respectively. Lasers operating at a wavelength of 2.5 μm have thresholds of 0.8 kW cm^{-2} for ns-pulsed optical excitation, and 1.1 kW cm^{-2} under cw optical excitation. The results offer a path towards monolithically integrated group IV laser sources on a Si photonics platform.

Introduction

Si-Ge-Sn alloys are a promising, enabling material system for the monolithic integration of both passive and active optoelectronic devices and circuits on Silicon¹. Silicon (Si) photonics presently relies on integration of III-V materials for emitters². Although such an approach has recently demonstrated some impressive progress, it still faces challenges like the wafer throughput, scalability and compatibility with the current Si complementary metal oxide semiconductor (CMOS) technology. The most successful route for laser action within group IV materials nowadays is based on germanium-tin (GeSn) semiconductors. The first demonstration of an optically pumped laser³ and subsequent developments to improve the performance in respect to threshold and operation temperature⁴⁻⁷, have shown the potential of these group IV materials for achieving Si-based light sources, the final ingredient for completing an all-inclusive nano-photonics CMOS platform. Furthermore, (Si)GeSn materials can help to extend the present Si photonics platform with a much broader application area than only near infrared data communication. In the short-wave to mid infrared region of 2–4 μm , in which GeSn laser emission has been obtained, potential applications including gas sensing for environmental monitoring and industrial process control⁸, lab-on-a-chip applications^{9,10} or infrared imaging for night vision and hyperspectral imaging¹¹ can be envisaged.

A Sn content increase in GeSn alloys modifies the energy of the electronic bands. The band-gap at Γ -point (E_{Γ}) reduces faster than the band-gap towards the L -valley (E_L), leading to a crossover from an indirect to a direct band-gap semiconductor at an Sn concentration of 8 at. %³. The lattice mismatch between Sn-containing alloys and the Ge buffer layer, the typical virtual substrate for their epitaxial growth, generates compressive strain in the grown layer, which counteracts the effect of Sn incorporation, decreasing the directness $\Delta E_{L-\Gamma} = E_L - E_{\Gamma}$. On the contrary, applying tensile strain will increase the directness.

Finding a proper balance between a moderate Sn content to minimize crystal defects and to maintain thermal stability of the GeSn alloy on one hand and making use of tensile strain on the other hand are the keys to bring lasing threshold and operation temperature close to application's requirements. The mainstream research to increase $\Delta E_{L-\Gamma}$ focuses on high Sn content alloys^{5,12}, obtained by epitaxy of thick strain-relaxed GeSn layers. A large directness is obtained, leading to higher temperature operation, although at the expense of steadily increasing laser threshold¹³. We have recently theoretically proposed an alternative approach, which is based on two key ingredients: employing moderate Sn content GeSn alloys, and inducing tensile strain in them¹⁴. This study indicated that, if a given directness is reached via tensile strain rather than by increasing Sn content, the material can provide a higher net gain. The underlying physics originates in the valence band splitting and lifting up of the light hole, *LH*, band above the heavy hole, *HH*, band. Its lower density of states (DOS) reduces the carrier density required for transparency, hence reduces the lasing threshold, as will be shown below.

GeSn alloys with a moderate Sn content offer a couple of advantages from the materials perspective. The epitaxial growth temperature, 375 °C compared to below 300 °C for high Sn content alloys, yields a better crystalline quality and lower defect density. Lattice mismatch, and therefore, the density of misfit dislocations at the GeSn/Ge interface scales with the Sn content¹⁵. Both types of defects strongly influence the carrier recombination dynamics^{16,17} and contribute to the high pumping levels necessary to reach lasing. Accordingly, laser thresholds of 100–300 kW cm⁻² were reported at 20 K for GeSn lasers with 12–14 at. % Sn^{4,18}, while ~MW cm⁻² values are required for very high Sn content alloys (>20 at. %) above 230 K^{7,12}.

The described material advantages and the underlying physics should then be combined with the technology able to induce tensile strain in GeSn alloys. Strain engineering is a mature Si technology employed to modify the electronic band structure of semiconductors¹⁹. In pure Ge, 1.7 % biaxial^{20,21} or 4.5 % uniaxial^{22–24} strain is required to energetically align the *L*- and Γ -valleys ($\Delta E_{L-\Gamma} = 0$), i.e. to reach crossover from an indirect to a direct semiconductor. Even higher strain is required to achieve the mandatory directness, $\Delta E_{L-\Gamma} > 150$ meV, for room temperature operation of a strained Ge laser. Although such high levels of tensile strain are technologically possible^{25,26}, they are challenging in a laser device geometry. Depending on Sn content, which can be chosen in the range of 5–8 at. %, significantly lower values of tensile strain are needed in GeSn alloys to achieve a sufficient directness¹⁴. However, in order to obtain laser with low pumping threshold, the impact of the defective GeSn/Ge interface region has to be removed. It is responsible for a considerable part of non-radiative recombination. The growth of hetero- and quantum well structures appears to be a suitable technology to separate the gain material from the defective interface¹⁷. Here, we focus on the impact of tensile strain and, for simplicity, we are using bulk GeSn layers. To remove the defective interface, the layer transfer method is applied, as used to fabricate GeSn on insulator (GeSnOI) structures. Due to the transfer, the defective part is at the top surface of the GeSn layer and can be easily removed by etching.

All GeSn lasers reported in the literature so far operate only under pulsed excitation, although continuous wave (cw) lasing is the key milestone required for accessing the full potential of GeSn for technologically useful optical devices.

In this work, we demonstrate both cw and pulsed lasing using microdisk cavities fabricated from initially indirect band-gap Ge_{0.946}Sn_{0.054} alloys. Tensile strain of 1.4 % is applied *ex-situ* to the GeSn layer, using all-around SiN_x stressors. The method relies on the formation of GeSnOI by wafer bonding and layer transfer, followed by under-etching so that the final cavity is supported by a metallic post, here Al, that acts as a heat sink. The combination of these factors, i.e. strain engineering, bulk defect density reduction, and improved heat removal, allows the demonstration of lasing in tensile strained GeSn with record low thresholds of 0.8 kW cm⁻² and 1.1 kW cm⁻² at 25 K in pulsed and cw operation regimes, respectively. The threshold is two orders of magnitude lower than previously reported for GeSn pulsed lasers, while no reports of cw lasing in GeSn are available.

Results

Material growth, characterization and cavity patterning. The GeSn layers were grown on Ge virtual substrates (Ge-VS) on 200 mm Si(100) wafers^{4,18} TRON TRICENT[®] reactor²⁷. Digermane (Ge₂H₆) and tin tetrachloride (SnCl₄) were used as precursors for elementary Ge and Sn, respectively. GeSn layers with thicknesses of 300 nm and Sn content of 5.4 at. % were grown at 375 °C. The layers were partially strain relaxed, with a residual compressive strain of -0.32 % as measured by X-Ray diffraction (Figure 1a). Details on material characterization can be found in the supplementary information (SI).

The GeSn layers were processed into microdisk cavities with all-around SiN_x stressors. The technology flow, developed for pure Ge²⁸ and adapted for GeSn thermal budget limitations²⁹, is presented in the SI. Yet, some key aspects are shown in Figure 1b. The stressor layer is a 350 nm thick SiN_x layer with an intrinsic stress of -1.9 GPa. An additional Al metal layer was added to the layer stack, in order to reduce heating during optical pumping^{30,31}. This is particularly important, since alloying of Ge with Sn strongly decreases the thermal conductivity of the alloy³². After GeSn bonding and removal of the donor wafer, the top 40 nm of the GeSn layer, containing the defective GeSn/Ge interface, was also removed. It was shown that this dense misfit network strongly reduces the photoluminescence of the layers at the onset of strain relaxation³³. Up to this step the compressive strain in the GeSn layer is preserved (Figure 1c,d). Tensile strain, coming from the SiN_x stressor underneath, is induced only by structuring the GeSn/ SiN_x layer stack (Figure 1b). The under-etching process, i.e. selective and local removal of Al, was optimized to maximize the tensile strain in the GeSn layer and have a wide Al post for heat sinking. Subsequently,

the suspended disks were conformally covered by a second 400 nm thick SiN_x stressor layer, leading to fully encapsulated GeSn disks, standing on Al posts (Figure 1b). This layer transfer technology and processing transforms the initial Ge_{0.946}Sn_{0.054} layer with residual compressive strain having an indirect band-gap into a microdisk exhibiting pronounced biaxial tensile strain and consequently a direct band-gap.

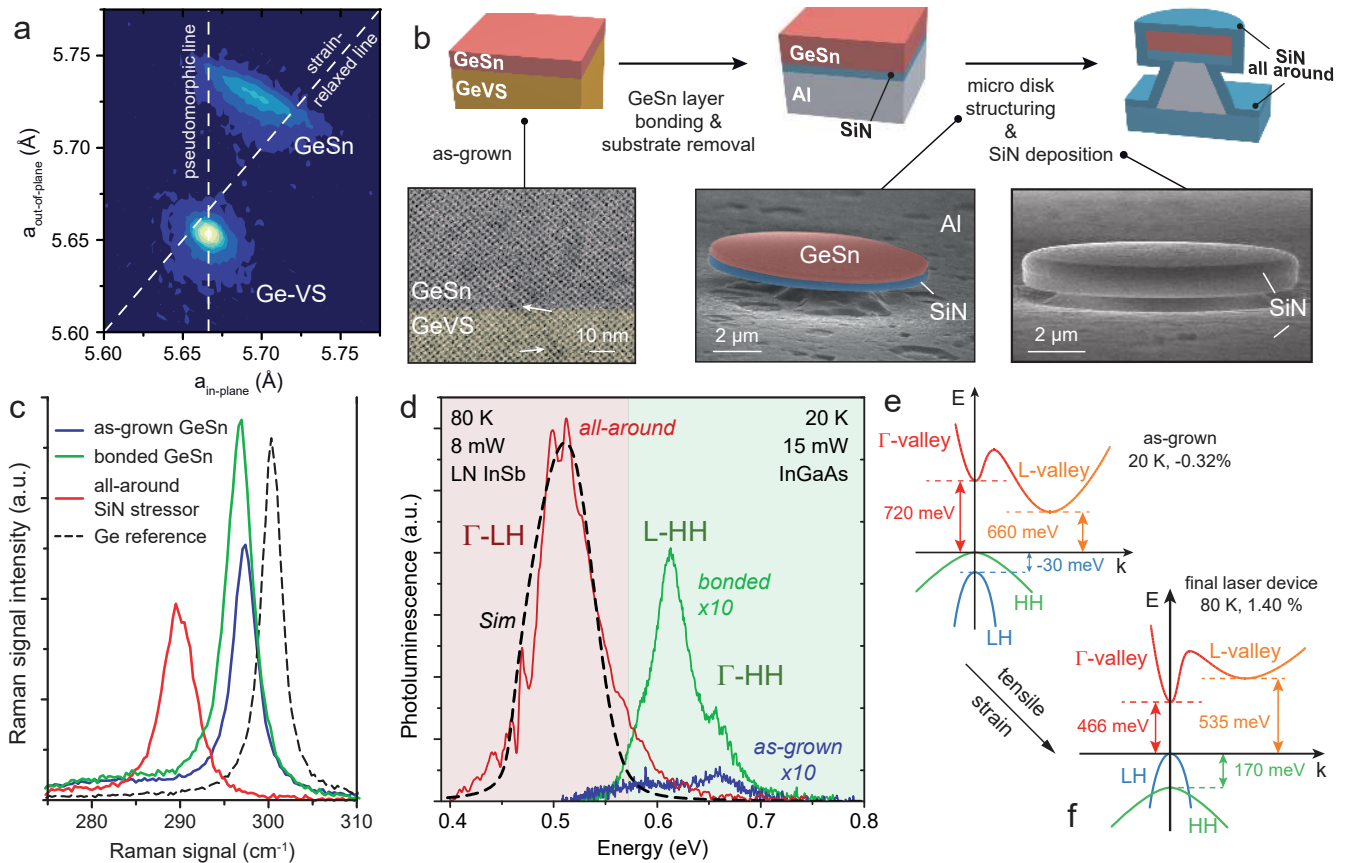


Figure 1. Structural and optical characterization. (a) X-Ray diffraction reciprocal space map for quantitative assessment of the layer strain (-0.32%). (b) Sketch of the processing steps. TEM image of the as-grown layer with strain releasing dislocations at the GeSn/Ge-VS interface. SEM images of the under-etched GeSn/SiN_x stack and the final laser structure with SiN_x all-around. (c) Raman spectra for three cases: as-grown layer, bonded (i.e. transferred) layer and all-around disk of $9\ \mu\text{m}$ diameter. Bulk Ge is used as reference. (d) PL spectra taken at 20 K for the as-grown and bonded GeSn layers (the bonded layer has the misfit dislocation network removed), and PL of patterned disk with all-around stressor at 80 K. The dotted line shows the simulated PL spectra of the final structure. The calculated band structure for the (e) indirect band-gap as-grown layer and (f) direct band-gap tensile strained GeSn layer.

Sample analysis

Raman spectroscopy was performed to follow the strain evolution during fabrication of GeSn microdisks. The positions of the Ge-Ge vibration modes in GeSn alloys in the as-grown sample (blue line), after bonding onto the host Si substrate (green line), and the final processed microdisk structure are shown in Figure 1c. The Raman modes of the unpatterned transferred layer and the as-grown layer, at $297.3\ \text{cm}^{-1}$ and $296.8\ \text{cm}^{-1}$, respectively, are very similar, within the experimental resolution of $0.5\ \text{cm}^{-1}$. Therefore, it can reasonably be assumed that the layer transfer process itself does not change the strain in the GeSn layer. However, after the processing of the final microdisk, a Raman shift of $-10.5\ \text{cm}^{-1}$ is detected. Using the equations from Ref.³⁴, including alloy disorder and strain effects, this Raman shift corresponds to a built-in biaxial tensile strain of 1.5% for the all-around embedded GeSn disk. Note that Raman spectroscopy probes only the in-plane strain within a small depth below the disk surface, while photoluminescence probes the whole disk volume, giving an average value of the strain, and is directly related to the band structure.²⁸

Photoluminescence (PL) experiments were conducted to assess the strain-induced band structure changes, as well as the quality improvement of the transferred layer. The PL signal from the as-grown GeSn layer is very weak, due to (i) the

indirect band-gap, with the conduction band energy splitting $\Delta E_{L-\Gamma} = -60$ meV, and (ii) the presence of defects at the GeSn/Ge interface. After the layer is transferred, these defects are removed and an increase in PL intensity is observed (Figure 1d). The PL signal is found in the same energy range, indicating again that the transferred layer maintains its compressive strain and, therefore, its indirect band-gap character with *L* and *HH* as conduction and valence band extrema, respectively. The optical transition at 0.61 eV is attributed to the recombination of electrons in the *L*-valley of the conduction band and holes near the Γ point of the *HH* valence band, thus across the fundamental indirect band-gap. Indirect carrier recombination dominates over the direct transitions, because almost 100 % of electrons at 20 K are in the *L*-valley. The shoulder of the PL signal around 0.66 eV is assigned to the direct transition, i.e. electrons and heavy holes around the Γ -point in *k*-space. Details on optical transition identification can be found in SI. PL spectra in Figure 1d for the as-grown and the transferred GeSn layers are taken under identical conditions with a sensitive InGaAs detector. This is emphasized because this, initially weakly-emitting, layer will become the active laser medium after inducing the tensile strain.

The major limitation for the GeSn emission efficiency, the indirect band-gap, is overcome by tensile strain turning it into a direct-gap semiconductor. Since the extended InGaAs detector has a cut-off wavelength of 2.4 μm , another set-up with a nitrogen cooled InSb detector, with a cut-off of 4.8 μm , is used for the fully processed microdisk device. Even though the InSb detector has a lower sensitivity, a strong increase of the integrated PL emission by 2 orders of magnitude compared to the as-grown layer is measured. The PL signal is strongly red-shifted, showing the peak emission around 0.50 eV which is attributed to the tensile strain of the final structure with the all-around SiN_x stressor. The band structure was modeled using **k**·**p** method, taking 5.4 at. % Sn and a band-gap of 465 meV of the strained film. The best fit to the experimental data in Fig. 1d is obtained for biaxial tensile strain of 1.4 %. This value is slightly smaller than the 1.5 % obtained from Raman spectroscopy. The discrepancy is attributed to the uncertainty of the parameters used in the two methods. The band structures of the as-grown and tensile strained GeSn are shown in Figure 1e and -f, respectively. In the final device, the tensile strain lifts the degeneracy of the *LH* and *HH* band, with *LH* becoming the fundamental valence band. The valence band splitting is $E_{LH} - E_{HH} = 170$ meV. More importantly, in the conduction band the tensile strain shifts the Γ -valley below the *L*-valley. The tensile strained GeSn thus becomes a direct band-gap material with a directness of $\Delta E_{L-\Gamma} = 70$ meV. Consequently, the pronounced enhancement of the PL intensity emission is due to the fundamental direct optical transition. The electrons recombine with *LH* at the Γ point in the center of the Brillouin zone. This transition is labelled as Γ -*LH* optical transition.

CW device results

In order to obtain stimulated emission, microdisk devices with a diameter of 9 μm were optically pumped using a μ -PL setup with 1550 nm wavelength cw pump laser focused on the sample surface into a 12 μm diameter spot (see Methods). PL emission spectra collected at various incident pump powers at 25 K are shown in Figure 2a. At low excitation levels, the microdisks produce a broad spontaneous emission background, attributed to $\Gamma \rightarrow LH$ direct transitions. By increasing the cw pump power from 0.2 mW to 0.8 mW, whispering gallery modes (WGM) develop and grow in intensity on top of the spontaneous emission. Higher excitation induces an exponential intensity increase of the main optical mode at 485 meV. At 2.3 mW pump power, the lasing emission is four orders of magnitude stronger than the background, as shown in the high resolution spectrum in Figure 2b. The two symmetric side lobes of the modes are only a measurement artifact, which stems from a finite range of sampling points due to the apodization of the interferogram.³⁵

The observation of a clear threshold in the light-in light-out (L-L) characteristic visible in Figure 2 c,d, the S-shape L-L characteristic (inset Figure 2d) and the collapse of the linewidth (Figure 2 c) unambiguously prove the onset of lasing. The emission energy at 25 K of the lasing mode at 485 meV corresponds to 2.55 μm wavelength. WGM simulations (see Methods) indicate that this mode is the transverse magnetic $\text{TM}_{20,1}$ mode. The intensity of this mode in the threshold region is displayed in Figure 2c as a function of incident pump power by the linear L-L characteristics. The observed narrowing is consistent with the Schawlow-Townes equations, which predict a decrease by a factor of two at the transition from incoherent to coherent emission. Note that the measured linewidth of 58 μeV is the smallest reported to date for any group-IV semiconductor lasers. The laser threshold, clearly separating the spontaneous and the amplified emission regimes, is extracted as 1.3 mW (Figure 2d). This value corresponds to a pump power density of 1.1 kW cm^{-2} . The dependence of the integrated signal on cw pumping power at different temperatures is also shown in Fig. 2d. The typical laser S-shape emission is shown in logarithmic scales in the inset. Below 45 K an unambiguous threshold can be observed, while no signature of lasing is detected above 45 K. A roll-over of the integrated emission occurs for pump powers above 5 mW. In III-V compounds this effect is typically associated with thermal effects, leading to a sharp laser emission quenching with further increase of temperature. However, in the case of GeSn microdisk laser under investigation, the directness $\Delta E_{L-\Gamma}$ is in the range of only 70 meV. In fact, band filling effects of the Γ -valley will reduce the electrons energy required for thermal (scattering) escape from Γ - into the *L*-valley even further. Therefore, a small increase in temperature or excitation power may lead to an exponential increase of this thermal escape, producing the observed roll-over. As will be discussed later, an increase in the electron population of the *L*-valley leads to a decrease of the total gain. Microdisks with diameter of 12 μm were also fabricated. The underetching is kept constant, leading

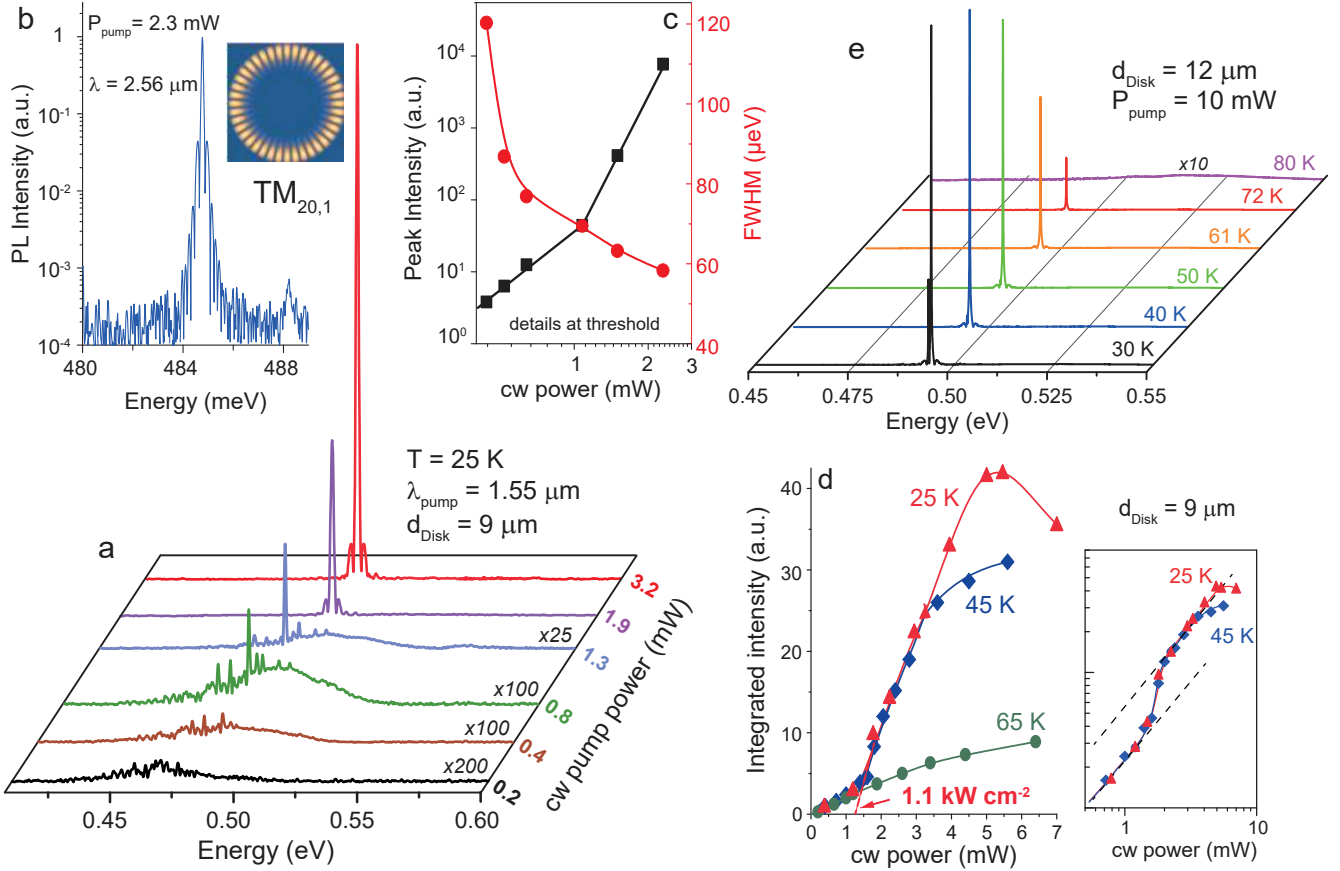


Figure 2. CW lasing from GeSn. (a) Emission spectra measured at 25 K for the 9 μm diameter disk under various cw excitation levels. (b) Lasing mode peak intensity above threshold in log scale, highlighting its high intensity compared to the spontaneous background emission. The intensity profile of the lasing mode, identified as $\text{TM}_{20,1}$, is shown in the inset. (c) Detailed behaviour at threshold: L-L curve of the peak intensity of the 485 meV laser mode (black) and its linewidth (red). (d) L-L curve of the integrated spectra at different temperatures (on logarithmic scales in the inset). Lasing threshold is extracted to be 1.3 mW (see SI), corresponding to 1.1 kW cm^{-2} . (e) PL spectra measured on a 12 μm diameter disk under cw pump power of 10 mW at various temperatures from 30–80 K showing lasing operation up to 72 K.

to same biaxial tensile strain in the GeSn suspended area, where the WGMs are formed. The laser emission at 489 meV, is only 4 meV higher than in 9 μm diameter disks. One major difference here is that the Al support pillar is much larger now, enabling a better heat dissipation. The 12 μm diameter disk can support the cw lasing up to 72 K. The PL spectra versus temperature are plotted in Figure 2e. The same laser threshold is obtained as for the smaller 9 μm diameter disks and increases with temperature, reaching about 5 mW at 72 K (details in SI). Estimation of the disk heating under optical pumping, using Finite Element Modeling (FEM)^{30,36}, can be found in the SI.

The PL spectra of a 9 μm diameter disk taken at excitation powers below the lasing threshold are shown in Figure 3a. Assuming a constant temperature of 25 K, spontaneous emission spectra were calculated for different carrier densities in order to reproduce the broadening of the emission and its blue shift when the pump power increases. The emission blue shift, observed experimentally when increasing the pump power, can be attributed to band filling effect inducing transitions at higher energies, since additional optical transitions occur at higher energies. Considering a band-gap of 465 meV the broadened PL spectra are well reproduced for carrier densities of $0.5 \times 10^{17} \text{ cm}^{-3}$, $1.5 \times 10^{17} \text{ cm}^{-3}$ and $2 \times 10^{17} \text{ cm}^{-3}$, which correspond to pump intensities of 0.17 kW cm^{-2} , 0.35 kW cm^{-2} and 0.71 kW cm^{-2} , respectively.

Under cw pumping, the steady state carrier density can be directly linked to the carrier lifetime, using the generation-recombination balance law $N = I\tau/(h\nu d)$, where I is the absorbed power density, τ the non-radiative recombination lifetime, $h\nu$ the pump photon energy and d the absorption depth. To obtain the absorbed power used for calculating carrier density and material gain, the incident power is multiplied by 0.65 to account for the disk surface reflectivity at 1550 nm wavelength. The extracted non-radiative lifetimes are 1.4 ns, 2.1 ns and 1.4 ns for carrier densities of $0.5 \times 10^{17} \text{ cm}^{-3}$, $1.5 \times 10^{17} \text{ cm}^{-3}$ and

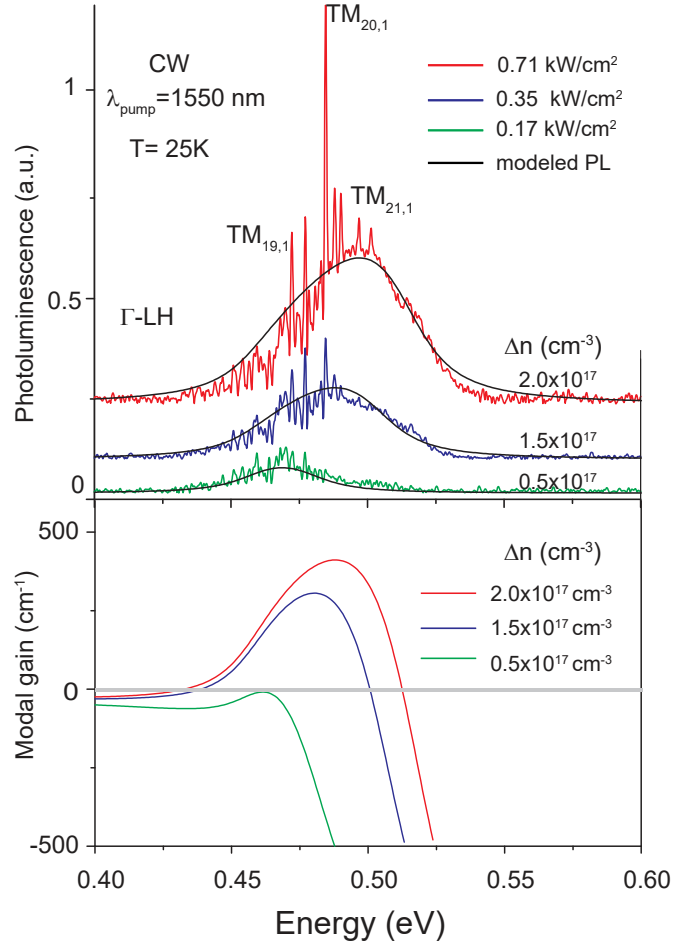


Figure 3. Carrier density at threshold and net gain (a) PL spectra below threshold, taken at 25 K under cw pumping of 0.2 mW, 0.4 mW and 0.8 mW. WGMs form on top of the spontaneous emission-dominated spectrum. The solid black lines are the calculated spontaneous emission spectra for different carrier densities. **(b)** Calculated modal gain for the carrier density values from (a).

$2 \times 10^{17} \text{ cm}^{-3}$, respectively. The obtained values, averaged to around 1.6 ns, are equivalent to those reported in Ref.³. However, even with comparable lifetimes, a clearly lower pumping threshold is here observed. This remarkable feature will be discussed in the next section.

The modal gain illustrated in Figure 3b was calculated for the carrier densities mentioned above, assuming steady-state conditions. The required parameters were obtained from the $\mathbf{k}\cdot\mathbf{p}$ band structure description, and are summarized in Methods. At a carrier density of $0.5 \times 10^{17} \text{ cm}^{-3}$ the positive gain regime is not reached, but the gain steeply increases with the carrier density. The modal gain maximum is observed at the lasing mode energy of 485 meV. Furthermore, gain broadening is observed for larger pumping intensity due to band filling effects. Note that the calculated modal gain might be overestimated, since it depends on unknown parameters such as homogeneous broadening. Nonetheless, these calculations indicate that modal gain can reach up to 400 cm^{-1} for carrier densities of $2 \times 10^{17} \text{ cm}^{-3}$.

Narrow whispering gallery modes appear in addition to the broad spectrum of spontaneous emission, clearly visible in Figure 3a. The modes at 472 meV, 485 meV and 497 meV are regularly spaced by 12–13 meV and can be assigned to fundamental $\text{TM}_{19,1}$, $\text{TM}_{20,1}$ and $\text{TM}_{21,1}$ modes, respectively. Other mode patterns in the spectrum can be attributed to higher radial index modes, with $n = 2$ and $n = 3$. The $\text{TM}_{19,1}$ mode is close to the band-gap, just a few meV apart. According to gain modelling it does not match the gain maximum. The $\text{TM}_{20,1}$ mode, at higher energy, here shows a better match. Thus the $\text{TM}_{20,1}$ mode will dominate the spectrum at high powers. This mode competition behaviour leads to a clear single-mode laser emission.

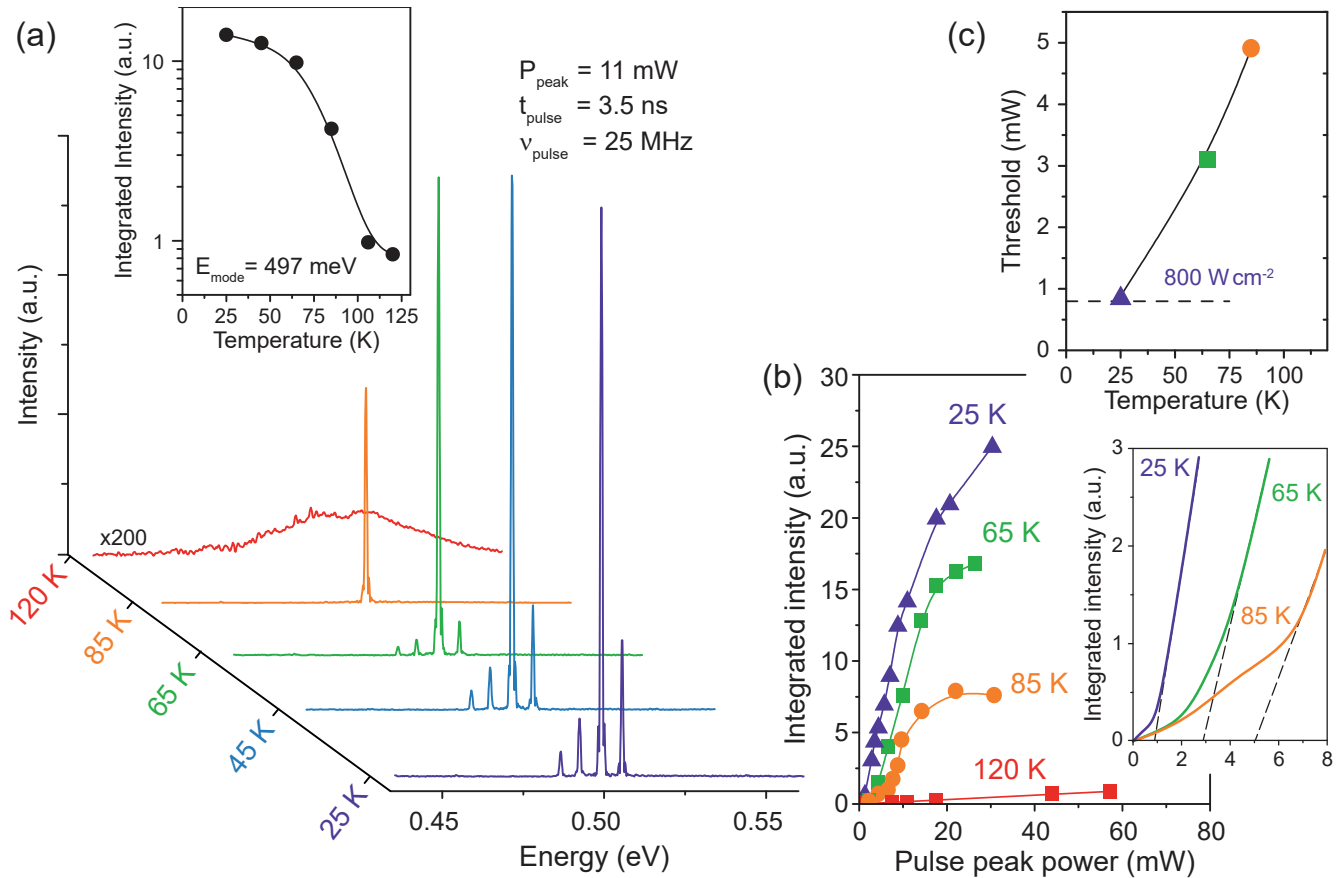


Figure 4. Pulsed laser. **a** Temperature dependence of light emission of a 9 μm diameter disk under pulsed peak power excitation of 11 mW. The inset shows the integrated PL signal for the laser mode at 497 meV. **b** L-L curves at 25 K, 65 K, 80 K and 120 K. No lasing is observed at 120 K. (inset) Zoomed view of L-L curves around threshold. **c** Lasing threshold as a function of temperature.

Pulsed device results

Since all the GeSn lasers reported in the literature were only operational under pulsed laser excitation, we also studied the properties of the present tensile strained GeSn microdisks. This enables a comparison of GeSn lasers with moderate Sn contents and tensile strain to those reported previously in the literature, having high Sn contents and residual compressive strain. Laser emission spectra taken at temperatures in the range of 25–120 K are shown in Figure 4a. 3.5 ns long pulsed excitation at a fixed peak pump power of 11 mW (1 mW average pump power) was here applied. Distinct differences from the cw excitation regime are observed. The laser spectra are multi-mode, with a dominant mode at 497 meV corresponding to a 2.49 μm emission wavelength. Mode assignment can be made by referencing to the spectra shown in Figure 3a. The lasing mode at the lowest energy corresponds to the one under cw operation at 485 meV. The dominant mode at 497 meV is also observed at the same energy in Figure 3a. From modelling of the whispering gallery modes, we can assign this mode to the transverse magnetic $\text{TM}_{21,1}$, as the free spectral range matches the expectation from modelling. The other two modes, at 488 meV and 502 meV, are assigned to modes with a higher order radial index, i.e. $\text{TM}_{17,2}$ and $\text{TM}_{18,2}$. The modes with radial number $n = 1$ are essentially un-shifted compared to those observed in cw regime in Figure 3a. Under pulsed excitation, there is a non-uniform spatial distribution of carriers, and possibly also a non-equilibrium distribution over the conduction band valleys, as well as a different temperature gradient compared to cw excitation. The non-uniform/non-equilibrium distribution explains the shift of gain to modes with higher radial order indices. In the pulsed regime, the gain profile may indeed be different from that in cw, enabling multi-mode lasing and favouring higher energy modes. At higher temperatures, the laser spectra become single-mode (Figure 4a), indicating a narrower frequency range of positive gain. However, more importantly, the maximum laser operation temperature in pulsed operation is almost two times higher than in cw regime.

The L-L characteristics for different temperatures are given in Figure 4b. Here, a thermal roll-over occurs at 85 K for 20 mW peak pumping power (1.8 mW average power), compared to 5 mW at 25 K under cw excitation. For pulsed operation at 25 K

a lasing threshold peak power of 0.9 mW is measured (inset of Figure 4b), which corresponds to a record low pump power density of 0.8 kW cm^{-2} . This pump power density is 250 times smaller than that of the best bulk GeSn microdisk laser reported in the literature. The threshold is temperature dependent, as shown in Figure 4c. A rise in temperature to 85 K increases the threshold power density to 4.2 kW cm^{-2} . At 120 K no lasing signature is observed anymore. The maximum temperature at which the gain should be still detectable depends on the carriers density as well. Simulations of the gain for an electron/hole density of $1 \times 10^{17} \text{ cm}^{-3}$ indicate that the gain in this material becomes quite small at 120 K. Taking parasitic losses like scattering on surface roughness into account, these simulation results match the experimental observation.

In this paragraph we qualitatively discuss the laser operation mode, maximum lasing temperature and threshold pump power density for GeSn layers under tensile strain, and benchmark the results against literature data.

In our experiment, where pumping is above the lasing threshold, the steady-state carrier density is expected to be nearly constant since the quasi-Fermi level is clamped by stimulated emission process. Although all electrons are generated in the Γ -valley, many of them will scatter into the L -valley. In particular, for a small $\Delta E_{L-\Gamma}$, here only 70 meV, and an energy difference between the quasi-Fermi level and the L -valley of only 40 meV, estimated at 25K for an electron-hole density of $2 \times 10^{17} \text{ cm}^{-3}$, a substantial amount of carriers will cool down/scatter into the L -valley. The intra- and inter-valley carrier scattering times, by phonon emission/absorption, are in the ps range while the thermal relaxation time for the disk is in the μs range. This implies an equilibrium carrier distribution in cw, at a lattice temperature above the nominal temperature, by about 20–30 K under 8 mW pump power (see SI). The scattering rates increase with temperature and with the decrease of $\Delta E_{L-\Gamma}$, increasing the carrier density in the L -valleys superlinearly with the pump power. This leads to a decrease of the gain since carriers in L -valleys only contribute to free carrier absorption without any contribution to gain. Moreover, as the temperature is increased, the carrier density is affected by increased non-radiative recombinations that decreases the overall gain (see SI). Consequently, a roll-over of the L-L spectrum at 25 K is observed for an excitation power exceeding 7 mW and, above 45 K, lasing is strongly quenched. These results hint to a heating of the electron bath by 40 K above the nominal sample temperature. It was experimentally observed that reducing the pump photon energy, and consequently reducing the lattice heating, leads to increased maximum operating temperatures by about 20 K^{12,17}. The role of the lattice heating is underlined by the experimental observation of operation temperature increase by almost 30 K for the 12 μm disks. The heat dispersion by the Al pillar is then better than for 9 μm disks.

Operating the same laser under pulsed excitation substantially reduces the thermal load, improving the temperature performance of the device. Laser quenching appears above 85 K for 9 μm disks and 100 K for 12 μm disks. The operation temperature increase for pulsed operation is only 15 K, about a half of that for cw operation. This indicates that cw lasing is much more sensitive to temperature than the pulsed operation. This may explain why no cw lasing was observed in compressively strained GeSn laser where the pumping powers were 100-200 times larger than in this work. Multi-mode and single-mode lasing for pulsed and cw pumping, respectively, is likely related to an incomplete wash-out of spatial hole-burning by carrier diffusion, together with a larger gain, for pulsed pumping³⁷.

Next we compare the results with those for Ge_{0.875}Sn_{0.125} microdisk laser with residual compressive strain, with a similar diameter of 8 μm ⁴, emitting at almost the same energy of $\sim 0.5 \text{ eV}$ (2.5 μm), having similar band-gap and directness $\Delta E_{L-\Gamma}$. With much stronger pump pulses, but 3 orders of magnitude smaller duty cycle, the average pump power and heat load there were lower, so it could tolerate a larger gain drop with increasing temperature, enabling a larger maximum operating temperature, of $\sim 130 \text{ K}$. The laser active layer in this work is the thinnest reported to date, less than a half of that in Ref.⁴ (260 nm vs. 560 nm), hence the mode overlap factors (affecting modal gain) also differ, being just 17 % here and 95 % in Ref.⁴. Even so, the GeSn device strained by SiN_x layers shows substantially lower threshold.

The main achievement of the presented GeSn laser is that it enables cw operation. This is a direct consequence of the strongly reduced threshold power, by at least a factor of 250, which allows continuous pumping while maintaining a moderate lattice temperature. This drastic improvement is attributed to three factors: (i) The large reduction of the valence band DOS ($\Delta E_{LH-HH} = 172 \text{ meV}$), warrants that the population inversion is achieved at a lower density of excited carriers. (ii) The modal gain of tensile strained GeSn is improved compared to unstrained GeSn with higher Sn content and the same $\Delta E_{L-\Gamma}$ ¹⁴. (iii) The non-radiative recombination rate is substantially reduced in lower Sn content alloys and even more so in the present structure with the defective epitaxial interface intentionally removed during processing. Defect reduction engineering is crucial, as previously reported for GeSn/SiGeSn quantum wells (QWs) lasers¹⁷.

The above discussion should provide some guidelines for improving the laser performance, by combining the advantages of the present structure with those from the previous GeSn laser research. An increase of the operating temperature up to 230 K was obtained by increasing the Sn content to 16 at. %⁷, and hence the directness $\Delta E_{L-\Gamma}$. Tensile strain can considerably reduce the requirement for high Sn contents. A tensile strain of 1.5 % in 10 at. % Sn alloy results in a very large Γ population at 300 K (see SI), and is, therefore, a viable route towards application-ready GeSn lasers. In addition, the use of SiGeSn/GeSn QWs heterostructures brings additional benefits from carrier confinement and energy quantization, enabling a threshold reduction by almost an order of magnitude for strain relaxed SiGeSn/GeSn QW¹⁷. Heterostructures as in Ref.³⁸, combined with tensile

strain, would strongly improve the carrier confinement at higher temperatures and, consequently, further decrease the threshold pump power density. QWs heterostructures yield a separation of the active region from interface defects without the use of a layer transfer technology, which is desirable for low-cost, high yield fabrication. In the present work bonding was used as a straightforward way to identify the intrinsic material optical properties. For tensile strain engineering, however, layer transfer is also not a mandatory solution, since several previous works have shown the feasibility of using a single stressor in cavities within a fully monolithic approach^{25,26,39}. Finally, the use of stressor layers has been shown to be compatible with an electrical pumping scheme⁴⁰ that could be incorporated into the presently used layout.

Conclusion

In summary, we have demonstrated a GeSn-based laser fully embedded in a SiN_x stressor conform layer. Starting with an indirect band-gap GeSn alloy we converted it, by inducing tensile strain, into a direct-gap optical gain material. Most importantly, cw and pulsed laser operation with ultra-low lasing thresholds of 0.8–1.1 kW cm⁻² are demonstrated. These values are significantly lower than any value reported for group-IV lasers, and are even comparable to those for epitaxially grown III-V InP lasers⁴¹, or InGaAs lasers bonded on Si wafers⁴², albeit the latter operate at room temperature. This achievement relies on using dilute GeSn alloys with just 5.4 at. % Sn, in contrast to the mainstream research focusing on 16–20 at. % Sn. While the lower Sn content decreases the $\Delta E_{L-\Gamma}$ splitting (directness), tensile strain compensates for that and, additionally, offers a reduced DOS by shifting the *LH* band above the *HH* band. In the present work, we combine the material quality advantage of low Sn content alloys and the physics of tensile strain with processing technology and thermal management, enabling lasing in low Sn-content alloys at record-low pumping powers and operating in a cw regime. Consequently, a viable route towards room temperature operation is predicted by combining modest Sn concentrations of ~10% with tensile strain >1% in the active layer.

Methods

Optical PL excitation was provided by an Nd:YAG laser at 1064 nm wavelength focused on the sample surface with a microscope objective, $\times 40$ and Numerical Aperture (NA) of 0.65, into a 5 μm diameter spot. Collection of emitted light was performed with the same microscope objective, and a beamsplitter was used to separate emission and excitation beam paths. In these experiments, we used an extended InGaAs detector to detect the luminescence. The high sensitivity, enabling the detection of low levels of infrared signals, was counterbalanced by the 2.5 μm wavelength cut-off due to the detector and objective transmission quenching.

Lasing experiments were performed using a μ -PL setup, where the cw pump laser beam at 1550 nm wavelength was focused on the sample surface into a 12 μm spot diameter by a $\times 40$ reflective objective with NA of 0.5 and working distance of 4 mm. The same objective was used for pumping and for collection of light emitted from the microdisk. A CaF₂ beamsplitter was used to separate the excitation and emission beam paths. The outgoing emission, collected from the objective, was coupled to a Fourier Transform Infrared (FTIR) spectrometer equipped with a CaF₂ beam splitter. The emission was detected by a nitrogen-cooled InSb photodetector, which has a cut-off wavelength 4.8 μm . The telecom wavelength pump laser was out-coupled from a single-mode fiber to free space using a hyperbolic mirror, the output fiber being clamped at the focal point of the mirror. The pump can be taken through a Mach-Zehnder modulator, controlled by an rf-pulse generator so that the pump beam power can be switched from cw to quasi-continuous and to pulsed mode. The same output from a single-mode fiber was used in both cases, cw or pulsed, so that switching from one pump mode to another did not induce any change of the beam waist or its alignment to the disk. The pulse shape under modulated excitation had 3.5 ns width and a repetition rate of 25 MHz. As discussed below, the pulse duration was longer than the non-radiative lifetime, so the optical excitation can be considered quasi-cw in this respect. The FTIR spectrometer resolution was set to 0.25 cm⁻¹ for line-width narrowing analysis of lasing mode around threshold otherwise it was set to 4 cm⁻¹.

Calculation of whispering gallery modes was performed by a 2D analytical model. The resonance wavelength of the cavity mode with azimuthal index m is calculated from the roots of m^{th} Bessel function $I_m(\frac{2\pi n_{\text{eff}}(\lambda)}{\lambda_{\text{res}}}a)$. The optical field is plotted at the resonant wavelength to obtain the corresponding radial number n of nodes along the disk radius. To account for modal dispersion of vertically confined modes, the effective index is introduced in the model, according to $n_{\text{eff}}(\lambda) = -0.6\lambda + 3.85$, where λ is the wavelength in μm . This expression was interpolated from 1D slab modelling of TM polarized waves, propagating in the GeSn layer. The energy of the TM_{20,1} mode is calculated to be 484.65 meV, in good agreement with the 485 meV experimental value.

Optical gain is calculated within the framework of parabolic band effective mass model, using the equation²⁸

$$g(\hbar\omega) = |D_{\Gamma,LH}^{TM}|^2 \int_0^{\infty} \rho_{LH}(E)(f_C(E) - f_V(E)) \frac{\frac{\Gamma_0}{2\pi}}{(\frac{\Gamma_0}{2})^2 + (E_{\Gamma,LH} + E - \hbar\omega)^2} dE,$$

where $\rho_{LH}(E)$ is the joint density of states involving the Γ conduction band and the LH valence band, and $|D_{\Gamma,LH}^{TM}|^2$ is the interband dipole matrix element. Γ_0 is the full width at half maximum of a Lorentzian function, which is here set to 25 meV to account for homogeneous broadening of interband transitions, while $f_C(E)$ and $f_V(E)$ are the Fermi-Dirac functions for electrons and holes. The density of states effective masses, used in the calculation, were $m_{\Gamma} = 0.036 m_0$, $m_L = 0.56 m_0$, and $m_{LH} = 0.05 m_0$, extracted from the **k.p** model¹⁴ of strained GeSn with 5.4 at. % Sn content and biaxial tensile strain of 1.4 %. The energy splitting $\Delta E_{L-\Gamma} = E_L - E_{\Gamma}$, $\Delta E_{LH-HH} = E_{LH} - E_{HH}$ and the band-gap $E_{\Gamma} - E_{LH}$ amount to 70 meV, 170 meV and 465 meV, respectively, according to **k.p** modeling and PL results. Note that the density of states effective masses differ only slightly from those in pure Ge, and we have therefore used the free carrier absorption model for pure Ge, assuming it would be very close to that for low Sn content GeSn alloy, in order to deduct it from the interband gain and find the net gain.

Acknowledgements

M.E.K. and A.E. thank Dr. Raffaele Colombelli and Prof. Adel Bousseksou for fruitful discussions and their help in mounting the PL setup with the FTIR spectrometer. The authors thank Dr. Gregor Mussler for XRD measurements. This work used knowledge acquired in the collaboration with Dr. Hans Sigg from PSI. This work was supported by the French RENATECH network, the French national research agency (Agence Nationale de la Recherche - ANR) through funding of ELEGANTE project (ANR-17-CE24-0015) and the Deutsche Forschungsgemeinschaft (DFG) via the project ‘‘SiGeSn Laser for Silicon Photonics’’. A.E. was supported by ANRT through a CIFRE grant. A. F. gratefully acknowledges funding within the ANR-16-CE09-0029-03 TIPTOP project.

Author contributions statement

All authors contributed to the work. P.B., M.E.K. and A.E. designed the device structure. M.E.K. and A.E. performed the strained disks fabrication with E.H., I.S., K.P., and G.P.. M.E.K. and A.E. performed the PL measurements and laser experiments with N.Z. and X.C.. K.P., G.P., I.S., N.v.d.D. and D.B. performed the structural analysis of the material. The GeSn layer was grown by D.B. and N.v.d.D. on substrates from J.-M.H.. The Raman analyses were performed by A.F. and R.O.. P.B., S.S. and Z.I. contributed to the modelling with M.E.K. and D.B.. The work was supervised by D.G., F.B., P.B., D.B. and M.E.K.. P.B., M.E.K., N.v.d.D., D.G and D.B. wrote the manuscript.

Competing interest

The authors declare no competing financial interests.

Data availability statement

The data that support the plots within this paper and other findings of this study are available from the corresponding author upon reasonable request.

Code availability statement

Finite element modeling was performed using a commercially available COMSOL software. All-other calculation codes were used in published works where model details are provided. The codes are not publicly available, any requests should be sent to the corresponding authors.

References

1. Soref, R. A., Buca, D. & Yu, S.-Q. Group IV Photonics - Driving Integrated Optoelectronics. *Opt. & Photonics News* **27**, 32–39, DOI: [10.1364/OPN.27.1.000032](https://doi.org/10.1364/OPN.27.1.000032) (2016).
2. Thomson, D. *et al.* Roadmap on silicon photonics. *J. Opt.* **18**, 073003 (2016).

3. Wirths, S. et al. Lasing in direct-bandgap GeSn alloy grown on Si. *Nat. Photonics* **9**, 88–92, DOI: [10.1038/nphoton.2014.321](https://doi.org/10.1038/nphoton.2014.321) (2015).
4. Stange, D. et al. Optically Pumped GeSn Microdisk Lasers on Si. *ACS Photonics* **3**, 1279–1285, DOI: [10.1021/acsphotonics.6b00258](https://doi.org/10.1021/acsphotonics.6b00258) (2016).
5. Reboud, V. et al. Optically pumped GeSn micro-disks with 16% Sn lasing at 3.1 μm up to 180 K. *Appl. Phys. Lett.* **111**, 092101, DOI: [10.1063/1.5000353](https://doi.org/10.1063/1.5000353) (2017).
6. Al-Kabi, S. et al. An optically pumped 2.5 μm GeSn laser on Si operating at 110K. *Appl. Phys. Lett.* **109**, 171105, DOI: [10.1063/1.4966141](https://doi.org/10.1063/1.4966141) (2016).
7. Thai, Q. M. et al. GeSn heterostructure micro-disk laser operating at 230K. *Opt. Express* **26**, 32500–32508, DOI: [10.1364/OE.26.032500](https://doi.org/10.1364/OE.26.032500) (2018).
8. Hodgkinson, J. & Tatam, R. P. Optical gas sensing: a review. *Meas. Sci. Technol.* **24**, 012004, DOI: [10.1088/0957-0233/24/1/012004](https://doi.org/10.1088/0957-0233/24/1/012004) (2013).
9. Sieger, M. & Mizaikoff, B. Toward On-Chip Mid-Infrared Sensors. *Anal. Chem.* **88**, 5562–5573, DOI: [10.1021/acs.analchem.5b04143](https://doi.org/10.1021/acs.analchem.5b04143) (2016).
10. Singh, V. et al. Mid-infrared materials and devices on a Si platform for optical sensing. *Sci. Technol. Adv. Mater.* **15**, 014603, DOI: [10.1088/1468-6996/15/1/014603](https://doi.org/10.1088/1468-6996/15/1/014603) (2014).
11. Razeghi, M. & Nguyen, B.-M. Advances in mid-infrared detection and imaging: a key issues review. *Reports on Prog. Phys.* **77**, 82401, DOI: [10.1088/0034-4885/77/8/082401](https://doi.org/10.1088/0034-4885/77/8/082401) (2014).
12. Dou, W. et al. Optically pumped lasing at 3 μm from compositionally graded gesn with tin up to 22.3%. *Opt. Lett.* **43**, 4558, DOI: [10.1364/OL.43.004558](https://doi.org/10.1364/OL.43.004558) (2018).
13. Zhou, Y. et al. Optically pumped gesn lasers operating at 270 k with broad waveguide structures on si. *ACS Photonics* **6**, 1434–1441, DOI: [10.1021/acsphotonics.9b00030](https://doi.org/10.1021/acsphotonics.9b00030) (2019). <https://doi.org/10.1021/acsphotonics.9b00030>.
14. Rainko, D. et al. Impact of tensile strain on low Sn content GeSn lasing. *Sci. Reports* **9**, 259, DOI: [10.1038/s41598-018-36837-8](https://doi.org/10.1038/s41598-018-36837-8) (2019).
15. Gencarelli, F. et al. Crystalline properties and strain relaxation mechanism of CVD grown GeSn. *ECS Transactions* **50**, 875–883, DOI: [10.1149/05009.0875ecst](https://doi.org/10.1149/05009.0875ecst) (2013).
16. Dou, W. et al. Investigation of GeSn Strain Relaxation and Spontaneous Composition Gradient for Low-Defect and High-Sn Alloy Growth. *Sci. Reports* **8**, 5640, DOI: [10.1038/s41598-018-24018-6](https://doi.org/10.1038/s41598-018-24018-6) (2018).
17. Stange, D. et al. GeSn/SiGeSn heterostructure and multi Quantum Well Lasers. *ACS Photonics* **5**, 4628–4636, DOI: [10.1021/acsphotonics.8b01116](https://doi.org/10.1021/acsphotonics.8b01116) (2018). <https://doi.org/10.1021/acsphotonics.8b01116>.
18. Du, W. et al. Study of si-based gesn optically pumped lasers with micro-disk and ridge waveguide structures. *Front. Phys.* **7**, 147, DOI: [10.3389/fphy.2019.00147](https://doi.org/10.3389/fphy.2019.00147) (2019).
19. Minamisawa, R. et al. Top-down fabricated silicon nanowires under tensile elastic strain up to 4.5%. *Nat. Commun.* **3**, 1096, DOI: [10.1038/ncomms2102](https://doi.org/10.1038/ncomms2102) (2012).
20. El Kurdi, M. et al. Direct Band Gap Germanium Microdisks Obtained with Silicon Nitride Stressor Layers. *ACS Photonics* **3**, 443–448, DOI: [10.1021/acsphotonics.5b00632](https://doi.org/10.1021/acsphotonics.5b00632) (2016).
21. Virgilio, M., Manganelli, C. L., Grosso, G., Pizzi, G. & Capellini, G. Radiative recombination and optical gain spectra in biaxially strained n-type germanium. *Phys. Rev. B* **87**, DOI: [10.1103/physrevb.87.235313](https://doi.org/10.1103/physrevb.87.235313) (2013).
22. Bao, S. et al. Low-threshold optically pumped lasing in highly strained germanium nanowires. *Nat. Commun.* **8**, 1845, DOI: [10.1038/s41467-017-02026-w](https://doi.org/10.1038/s41467-017-02026-w) (2017). [1708.04568](https://doi.org/10.1038/s41467-017-02026-w).
23. Süess, M. J. et al. Analysis of enhanced light emission from highly strained germanium microbridges. *Nat. Photonics* **7**, 466–472, DOI: [10.1038/nphoton.2013.67](https://doi.org/10.1038/nphoton.2013.67) (2013).
24. Armand Pilon, F. T. et al. Lasing in strained germanium microbridges. *Nat. Commun.* **10**, 2724, DOI: [10.1038/s41467-019-10655-6](https://doi.org/10.1038/s41467-019-10655-6) (2019).
25. Ghrib, A. et al. Control of tensile strain in germanium waveguides through silicon nitride layers. *Appl. Phys. Lett.* **100**, 201104, DOI: [10.1063/1.4718525](https://doi.org/10.1063/1.4718525) (2012).
26. Capellini, G. et al. Strain analysis in SiN/Ge microstructures obtained via Si-complementary metal oxide semiconductor compatible approach. *J. Appl. Phys.* **113**, 013513, DOI: [10.1063/1.4772781](https://doi.org/10.1063/1.4772781) (2013).

27. von den Driesch, N. et al. Direct bandgap group IV epitaxy on Si for laser applications. *Chem. Mater.* **27**, 4693–4702, DOI: [10.1021/acs.chemmater.5b01327](https://doi.org/10.1021/acs.chemmater.5b01327) (2015).
28. Ghrib, A. et al. All-Around SiN Stressor for High and Homogeneous Tensile Strain in Germanium Microdisk Cavities. *Adv. Opt. Mater.* **3**, 353–358, DOI: [10.1002/adom.201400369](https://doi.org/10.1002/adom.201400369) (2015).
29. Zaumseil, P. et al. The thermal stability of epitaxial gesn layers. *Appl. Phys. Lett. Mater.* **6**, 076108, DOI: [10.1063/1.5036728](https://doi.org/10.1063/1.5036728) (2018).
30. Elbaz, A. et al. Solving thermal issues in tensile-strained Ge microdisks. *Opt. Express* **26**, 28376–28384, DOI: [10.1364/OE.26.028376](https://doi.org/10.1364/OE.26.028376) (2018).
31. Elbaz, A. et al. Germanium microlasers on metallic pedestals. *APL Photonics* **3**, 106102, DOI: [10.1063/1.5025705](https://doi.org/10.1063/1.5025705) (2018).
32. Uchida, N. et al. Carrier and heat transport properties of polycrystalline gesn films on sio₂. *Appl. Phys. Lett.* **10**, 232105, DOI: [10.1063/1.4937386](https://doi.org/10.1063/1.4937386) (2015).
33. Pezzoli, F., Giorgioni, A., Patchett, D. & Myronov, M. Temperature-dependent photoluminescence characteristics of GeSn epitaxial layers. *ACS Photonics* **3**, 2004–2009, DOI: [10.1021/acsphotonics.6b00438](https://doi.org/10.1021/acsphotonics.6b00438) (2016).
34. Cheng, R. et al. Relaxed and strained patterned germanium-tin structures: A raman scattering study. *ECS J. Solid State Sci. Technol.* **2**, P138–P145, DOI: [10.1149/2.013304jss](https://doi.org/10.1149/2.013304jss) (2013).
35. Rabolt, J. F. & Bellar, R. The nature of apodization in fourier transform spectroscopy. *Appl. Spectrosc.* **35**, 132–135, DOI: [10.1366/0003702814731987](https://doi.org/10.1366/0003702814731987) (1981).
36. El Kurdi, M. et al. Tensile-strained germanium microdisks with circular Bragg reflectors. *Appl. Phys. Lett.* **108**, 091103, DOI: [10.1063/1.4942891](https://doi.org/10.1063/1.4942891) (2016).
37. Sargent, M. Theory of a multimode quasiequilibrium semiconductor laser. *Phys. Rev. A* **48**, 717–726, DOI: [10.1103/PhysRevA.48.717](https://doi.org/10.1103/PhysRevA.48.717) (1993).
38. Stange, D. et al. Short-wave infrared leds from gesn/sigesn multiple quantum wells. *Optica* **4**, 185–188, DOI: [10.1364/OPTICA.4.000185](https://doi.org/10.1364/OPTICA.4.000185) (2017).
39. Ghrib, A. et al. Tensile-strained germanium microdisks. *Appl. Phys. Lett.* **102**, 221112, DOI: [10.1063/1.4809832](https://doi.org/10.1063/1.4809832) (2013).
40. Prost, M. et al. Tensile-strained germanium microdisk electroluminescence. *Opt. Express* **23**, 6722–6730, DOI: [10.1364/OE.23.006722](https://doi.org/10.1364/OE.23.006722) (2015).
41. Wang, Z. et al. Novel Light Source Integration Approaches for Silicon Photonics. *Laser & Photonics Rev.* **11**, 1700063, DOI: [10.1002/lpor.201700063](https://doi.org/10.1002/lpor.201700063) (2017). [1610.06300](https://doi.org/10.1610.06300).
42. Seifried, M. et al. Monolithically Integrated CMOS-Compatible III–V on Silicon Lasers. *IEEE J. Sel. Top. Quantum Electron.* **24**, 1–9, DOI: [10.1109/JSTQE.2018.2832654](https://doi.org/10.1109/JSTQE.2018.2832654) (2018).

Supplementary information

Ultra-low threshold continuous-wave and pulsed lasing in tensile strained GeSn alloys

Anas Elbaz^{1,2}, Dan Buca^{3,*}, Nils von den Driesch^{3,4}, Konstantinos Pantzas¹, Gilles Patriarche¹, Nicolas Zerounian¹, Etienne Herth¹, Xavier Checoury¹, Sébastien Sauvage¹, Isabelle Sagnes¹, Antonino Foti⁵, Razvigor Ossikovski⁵, Jean-Michel Hartmann⁶, Frédéric Boeuf², Zoran Ikonc⁷, Philippe Boucaud⁸, Detlev Grützmacher^{3,4}, and Moustafa El Kurdi^{1,*}

¹ Center for Nanoscience and Nanotechnology, C2N UMR 9001, CNRS, Université Paris Sud, Université Paris Saclay, 91120 Palaiseau, France

² STMicroelectronics, Rue Jean Monnet 38054 Crolles, France

³ Peter Grünberg Institute (PGI 9) and JARA-Fundamentals of Future Information Technologies, Forschungszentrum Juelich, 52428 Juelich, Germany

⁴ JARA-Institute Green IT, RWTH Aachen, 52062 Aachen, Germany

⁵ LPICM, CNRS, Ecole Polytechnique, Université Paris-Saclay, 91128 Palaiseau, France

⁶ CEA, LETI and Univ. Grenoble Alpes, 38054 Grenoble, France

⁷ Pollard Institute, School of Electronic and Electrical Engineering, University of Leeds, Leeds LS2 9JT, UK

⁸ Université Côte d'Azur, CNRS, CRHEA 06560 Valbonne, France

*corresponding author: moustafa.el-kurdi@u-psud.fr, d.m.buca@fz-juelich.de

Table of contents:

- 1. Material characterization**
- 2. Processing and strain engineering**
- 3. Microdisk emission for different strain / technology steps**
- 4. Photoluminescence comparison and optical transitions assignment**
- 5. Thermal heating modelling**
- 6. Lasing spectra and threshold analysis**
- 7. Modal gain assuming SRH model**
- 8. Steady-state electron distribution in conduction band versus temperature**

1. Material characterization

Transmission electron microscopy (TEM) was used to investigate the crystalline and structural quality of the GeSn layer. A lamella was prepared using focused ion beam (FIB) and observed in a FEI Titan TEM microscope operating at 200 keV. Figure SI-1a shows a high-angle annular dark field (HAADF) Scanning TEM (STEM) micrograph of the GeSn layer. The 260 nm thick GeSn layer is partially relaxed through the formation of dislocations at the Ge/GeSn interface. These dislocations are localized within the first 20 nm of the GeSn layer as shown in the dark-field TEM micrograph in Figure SI-1b. No threading dislocations (TDs) were observed in TEM micrograph, so the lower limit for the TDs density is taken equal to the TDs density in the Ge-VS, $1 \times 10^7 \text{ cm}^{-2}$. A detailed analysis of TD density in Ge-VS was performed in Ref. [1].

The composition of the layer was measured by Rutherford Backscattering Spectrometry (RBS) and energy dispersive X-ray (EDX) spectroscopy. The plot in Figure SI-1c shows the results of these measurements along the growth direction. The average composition of the layer is 5.4 at.% of Sn, in agreement with Rutherford Backscattering Spectrometry (not shown here). A small gradient of Sn content of 0.7 % seems to be present along the growth direction, attributed to the strain relaxation of the layer. The GeSn layer is, therefore, slightly richer in Sn close to the surface contributing to carrier diffusion from the defective Ge/GeSn interface region towards the layer interior.

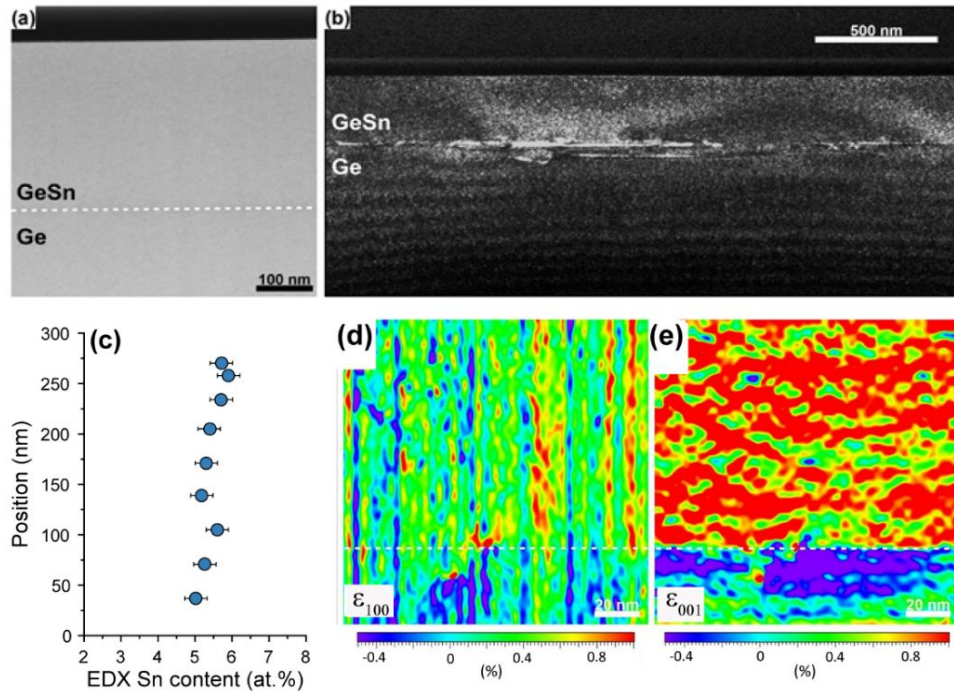


Figure SI-1. (a) High-angle annular dark field STEM micrograph of the as-grown 260 nm GeSn layer. (b) Dark-field TEM micrograph showing the presence of dislocations at the interface. (c) EDX line-scan along the growth direction, indicating an average Sn content of 5.4 at.%. A slight gradient of -0.7 at.% over 260 nm of the GeSn layer depth is observed. (d), (e) Strain mapping in the in-plane and out-of-plane directions, as obtained from Geometric Phase Analysis using bright field-STEM. The average in-plane and out-of-plane deformation with respect to Ge are $0.3\% \pm 0.3\%$ and $0.9\% \pm 0.5\%$, respectively. The (in-

plane) material strain calculated from these data is $-0.5\% \pm 0.3\%$.

Geometric Phase Analysis (GPA) was used to evaluate the strain distribution in the GeSn layer, delivering information on local strain with respect to the Ge-VS template. The findings are summarized in Figure SI-1d,e. The average in-plane deformation with respect to Ge is $0.3\% \pm 0.3\%$ while the out-of-plane one is $0.9\% \pm 0.5\%$, showing that GeSn has a tetragonal structure, being partially strain relaxed. The strain calculated from the lattice deformation (w.r.t. cubic GeSn crystal) for Sn content of 5.4 at.% is $-0.5\% \pm 0.3\%$, in reasonable agreement with XRD measurements (Figure 1 in the manuscript). The Z contrast of the GeSn layer is highly homogeneous, indicating that Sn atoms are evenly distributed.

2. Processing and strain engineering

The GeSn layers were processed into microdisks, embedded in a silicon nitride (SiN_x) stressor. The process, somewhat similar to that used for the fabrication of SOI substrates, was adapted to take three aspects into account: i) a stressor layer is included; ii) a heat sink layer is added; and iii) the materials/processes are chosen such that their deposition/processing temperature is below the growth temperature of the GeSn layer. The technological flow is schematically illustrated in Figure SI-2. On the as-grown GeSn on Ge-VS, a 350 nm thick SiN_x layer is deposited by plasma-enhanced chemical vapor deposition (PECVD), followed by 1 μm of aluminum (Al), deposited by e-beam evaporation (Fig. SI-2a). While multiple choices, such as SiO_2 - SiO_2 or Al-Al, are available for bonding, Au-Au bonding process was used in this proof-of-concept work. In order to avoid Au diffusion into Al during bonding at 320°C , a 100 nm SiN_x diffusion barrier was deposited by PECVD. The layers stack prior bonding is shown in Fig SI-2b. The total thermal budget for bonding and subsequent annealing, to increase the bonding strength, was maintained low enough to ensure the integrity of the GeSn layer by avoiding Sn segregation. Additionally, further relaxation of the GeSn layer is avoided.

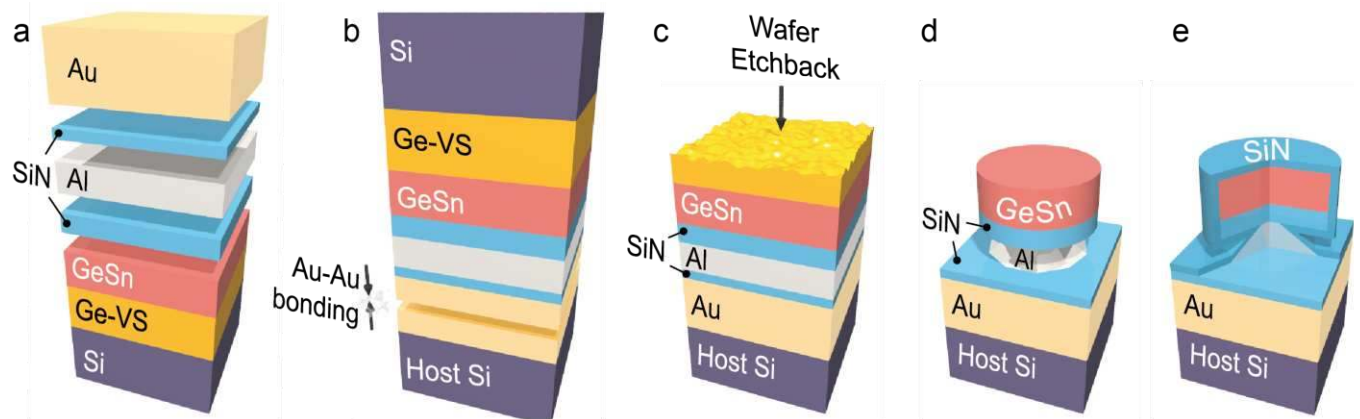


Figure SI-2: (a)-(d) Schematic view of the process flow, illustrating different fabrication steps of the strained GeSn disk. (a) Layer stack prior to bonding. (b) Bonding process. (c) Back-etching of the donor wafer. (d) Formation of the suspended disk by under-etching of the Al layer. At this step the strain from the bottom SiN stressor is transferred into the GeSn. (e) Final device structure: GeSn embedded in SiN .

Most of the Si substrate is removed by chemical mechanical polishing (CMP) down to 50 μm thickness followed by a selective wet etching of the remaining Si substrate. The Ge-VS layer acts as etch-

stop, having a very large etch selectivity versus Si in KOH wet chemical solution. A sulfur hexafluoride (SF_6) plasma is then used to remove the 2.5 μm thick Ge-VS (Figure SI-2c). At this step, about 40 nm of the GeSn layer, including the defective interface with Ge-VS, is also etched away. The GeSn layer thickness is reduced from 300 nm down to 260 nm. This transferred layer is then processed by standard lithography to define microdisk mesas with diameters in the range 4-9 μm . The mesas were etched into the GeSn/ SiN_x stack down to Al layer by Cl_2 plasma in a reactive ion etching system. The choice of Al for the metal was dictated by the high selectivity of KOH in etching Al versus GeSn and SiN_x , allowing for a precise under-etch control and, thus, tuning of the strain transferred into the GeSn layer. At the same time, large Al pillars are targeted to allow for an efficient heat sink. The suspended microdisk structure is shown in Fig. SI-2d. Once the metallic post was defined, a second SiN_x stressor layer (intrinsic stress of -1.9 GPa) is conformally deposited by PECVD, resulting in a GeSn microdisk embedded in SiN_x (Figure SI-2e). The top SiN_x is 400 nm and the bottom layer 350 nm thick.

3. Microdisk emission for different strain / technology steps

From the as-grown layer to the all-around disk different strain condition can be obtained. We can indeed fabricate the disk directly from the as-grown layer, then one should get a strain-free suspended GeSn layer cavity. A detailed analysis of strain in such a structure was performed in Ref. [2]. As shown in figure SI-3, with the material being an indirect band gap semiconductor the lasing cannot be reached, even under high pulsed pump power.

The next device is obtained following the steps shown in Fig SI-2, ending with the structure in FigSI2-d. The result is GeSn layer bonded on a SiN_x layer. The PL of the microdisk shows a red shift and a strong enhancement of the emission as compared to the as-grown layer disk. The red shift is a signature of tensile strain induced by the underlying SiN_x after patterning. In this case no laser effect can be obtained, either. The tensile strain is expected to be highly inhomogeneously distributed both along the disk diameter and across the layer depth. A detailed analysis of single side stressor layer on the disk is performed in Ref. [3]. FEM analysis shows that the average biaxial tensile strain in the layer is 0.5%, with the maximal strain of 0.8% close the GeSn/ SiN interface. In this strain configuration we were not able to get lasing, although the defects removal has been performed. Finally after the formation of an all-around SiN structure, by additional deposition of a second 400 nm SiN_x stressor layer on top of the previous structure, the lasing is achieved. The tensile strain reaches 1.4%, and has a highly homogenous volume distribution. This is the case discussed in the manuscript.

The results presented above referred to a $\text{Ge}_{0.946}\text{Sn}_{0.054}$ layer that is an indirect gap semiconductor for as-grown bulk conditions. The processing performed here can, however, offer laser emission for other (Sn composition - strain value) combinations, if it turns into a direct bandgap semiconductor and close to it.

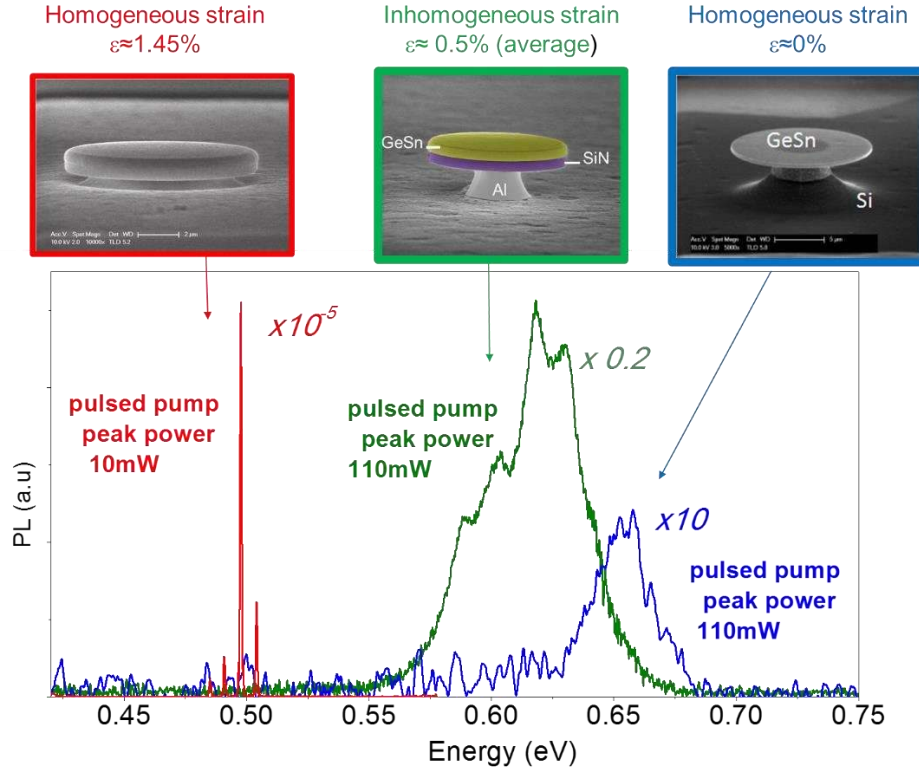


Figure SI-3: Photoluminescence analysis under pulsed pumping for different strain conditions in the GeSn layer used in this work i) suspended relaxed disk, ii) transferred layer with a single-bottom side SiN_x layer, iii) GeSn encapsulated in the all-around SiN_x stressor.

4. Photoluminescence comparison and optical transitions assignment

Figure 1 in the manuscript shows PL emission of the layer in the as-grown and bonded (but still unpatterned) form, measured by a highly sensitive InGaAs detector. For measurements of the final, tensile-strained device, a liquid nitrogen cooled InSb detector with a longer cut-off wavelength was used. Here we show the PL emission of the bonded layer and the final structure, GeSn disk embedded in SiN layers, using the InSb detector (Figure SI-4). This detector's sensitivity is, however, lower than that of InGaAs, making it less suitable for detection of emission from the as-grown layer. A large red-shift and a strong PL emission enhancement (about two orders of magnitude) are observed. These changes are attributed to a tensile strain induced band-gap narrowing and to the change from an indirect to direct character of the fundamental band-gap.

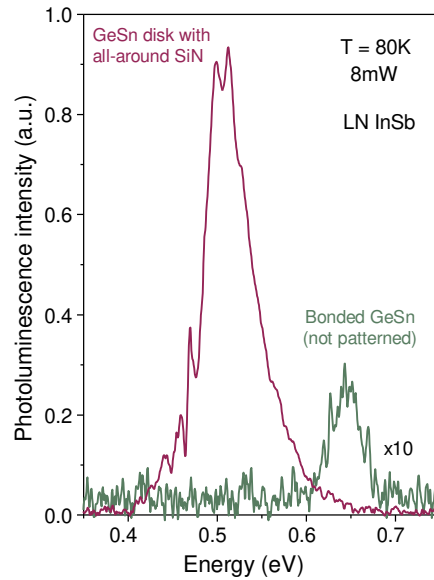


Figure SI-4: The PL emission at 80K of the GeSn layer: (green) after bonding (no strain transfer) and GeSn/Ge-VS interface etch, the direct transition Γ -HH dominates the spectrum; (pink) final structure: tensile strained GeSn embedded in SiN.

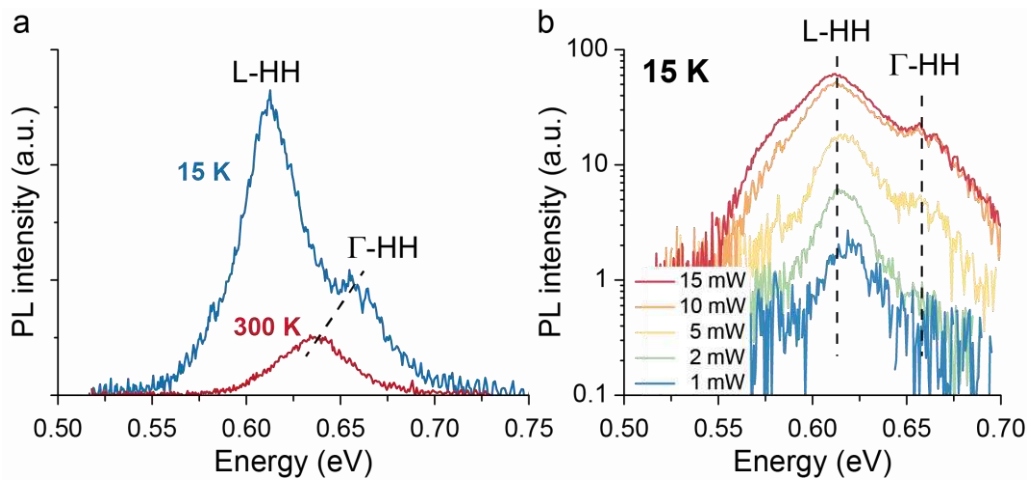


Figure SI-5: (a). Temperature dependence of the PL spectra of the bonded layer. The indirect transition L-HH dominates at 20K and the direct transition Γ -HH at 300K. (b) PL power dependence of the layer at low temperature, 15K.

In thin layers the PL at room temperature is dominated by the direct transitions for both indirect and direct bandgap semiconductors. In our case, with the compressive $\text{Ge}_{0.946}\text{Sn}_{0.054}$ layer, this is the Γ -HH optical transition. The major difference in PL between indirect and direct semiconductors is seen at low T and through the temperature behaviour. At cryogenic temperatures, the electrons occupy the lowest energy band, which is the L -valley for an indirect semiconductor and Γ -valley for a direct one. For our indirect GeSn compressively strained layer at 15K the main PL emission comes from the fundamental L-HH optical transition. The Γ -HH optical transition can be observed when the Γ -valley starts to be populated. This can be obtained:

- 1- Under high pumping conditions. This is shown in Fig. SI-5b. For our $\text{Ge}_{0.946}\text{Sn}_{0.054}$ layer this happens above 5mW.
- 2- Increasing the temperature. The electrons will be thermally activated to populate the Γ -conduction band. This thermal activation to direct conduction band occurs already at 80K due to the small energy difference between the L- and the Γ -valley, as extracted from the k.p modeling. Also very important is that the oscillator strength for direct transition is orders of magnitude larger than for the indirect transition. This makes the direct transition dominate over the indirect one at 80K and above.

Based on the above PL temperature behaviour we can conclude that the $\text{Ge}_{0.946}\text{Sn}_{0.054}$ layer under -0.32% compressive strain is an indirect semiconductor and assign the peak at 0.61 eV to the indirect L-HH fundamental optical transition and the higher energy peak at 0.66 eV to the Γ -HH direct optical transition. This energy difference of 50 meV is comparable to the Γ -L energy difference of 60 meV predicted by modeling.

5. Thermal heating modeling

Modelling of the thermal heat distribution inside the GeSn disk under optical pumping was performed using the same procedure, based on Finite Element Modeling (FEM), as in Ref. [4]. The pump power absorbed by the active layer is set as a homogeneous heat source distributed on the disk surface. A factor of 0.65 applied to the incident power takes into account the GeSn surface reflectivity at the pump wavelength of 1550 nm. Under 8 mW of incident power focused into a 12 μm spot diameter the intensity is 7.1 kW/cm^2 . The all-integrated absorbed power by the 9 μm diameter is thus 2.9 mW within the active GeSn layer, out of the total cw incident power of 8 mW. We assume that all the absorbed power is converted into heat in the disk. The FEM modeling results are shown in figure SI-6a. The data for GeSn thermal conductivity are scarce in the literature, but Sn alloying generally induces a significant drop in thermal conductivity due to mass disorder induced phonon scattering. In Fig SI-6b the modelling was performed for GeSn thermal conductivities of 1 $\text{Wm}^{-1}\text{K}^{-1}$, 2 $\text{Wm}^{-1}\text{K}^{-1}$ and 10 $\text{Wm}^{-1}\text{K}^{-1}$. The thermal conductivity of elemental Ge is 58 $\text{Wm}^{-1}\text{K}^{-1}$.

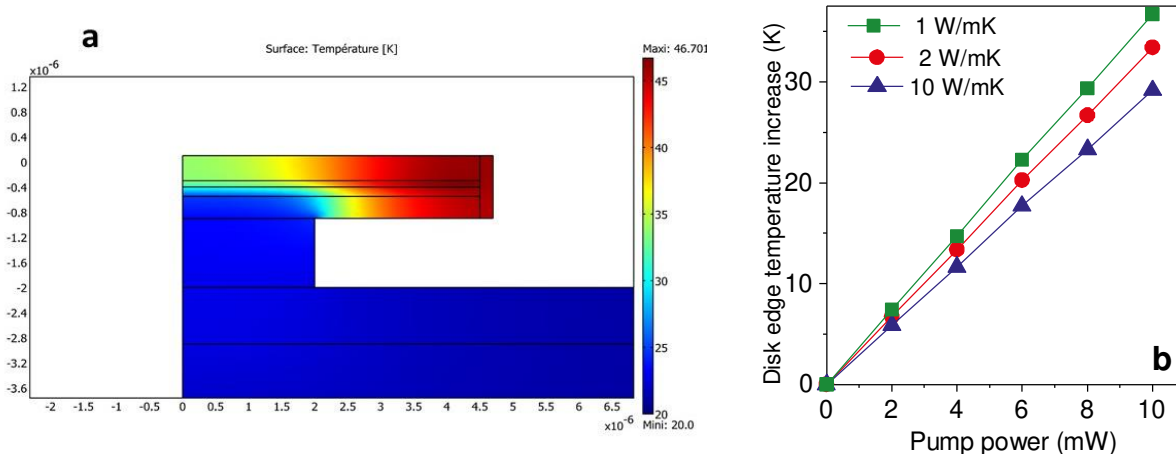


Figure SI-6: (a) Finite element modeling of temperature in the microdisk under incident pump power

of 8 mW. (b) Maximum temperature, at the disk edge, as a function of incident pump power for different GeSn thermal conductivities.

In Fig SI-6b the maximum temperature at the disk edge, where the whispering gallery modes form, is shown for different thermal conductivities. For our case of 9 μm diameter disks, a temperature increase of about 30 K under 8 mW pump power, i.e. 7.1 kW/cm^2 intensity, is found. The modeling is performed assuming a continuous heat source, and the results represent the steady-state temperature. Under pulsed pumping, the pulse duration is only 3.5 ns, very short compared to heat transfer rates out of the disk, which are in the μs range. One can thus take that the temperature reached in pulsed regime scales with the duty cycle, i.e. for a given pulsed peak power the heating is much lower than in cw. Therefore, the temperature increase under pulsed excitation, as used in this work, is estimated to be below 10 K, for pulsed peak power range of 0-100 mW. Note that due to unknown thermal transport parameters in GeSn alloy, this value should be taken as a rough estimate.

6. Lasing spectra and threshold analysis

The threshold extraction for the 9 μm disk at 20K under cw excitation and for the 12 μm diameter disk under both cw and pulsed excitations is shown in Fig SI-7 a-c. The same fabrication method was used, and also the same etching time as for the 9 μm diameter disk, to allow identical under-etch of the GeSn disk. The main difference is then only in the size of the Al pillar, directly related to the disk heat dissipation. The result is an increase of the cw lasing temperature from 45K for the 9 μm disk to 72K for the 12 μm disk. This is an increase by almost 30K for cw pumping and only 15K for pulse pumping. This indicates that cw lasing is more temperature sensitive than the pulsed lasing. In our case, the cw lasing thresholds for the 9 μm and 12 μm disk are almost identical at 20-30K. The cw and pulsed thresholds, similar at 20K, have however different temperature behaviour, and the lasing quenches faster for the cw laser. Note that the energy deposited in the disk by cw optical pumping is 11 times higher than in the pulsed pumping mode.

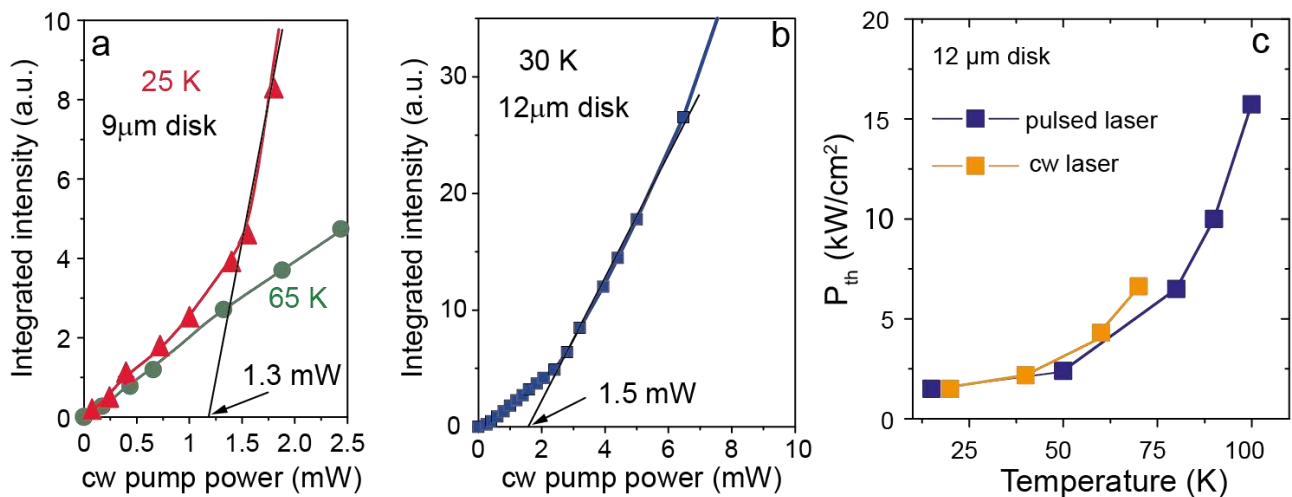


Figure SI-7: Threshold analysis for: (a) the 9 μm diameter disk under cw pumping, and (b) for the 12 μm diameter disk, showing equivalent lasing thresholds, and (c) Lasing threshold obtained for the 12 μm disk as a function of temperature and under cw and pulsed pumping. The maximum lasing operation temperature is 72 K under cw, and 100K under pulsed excitation.

The power dependence of PL emission spectra from a 12 μm disk, at the temperature of 72K are presented in Fig SI-8a. The light-in-light-out characteristics at 72K is plotted in Fig. SI-8b.

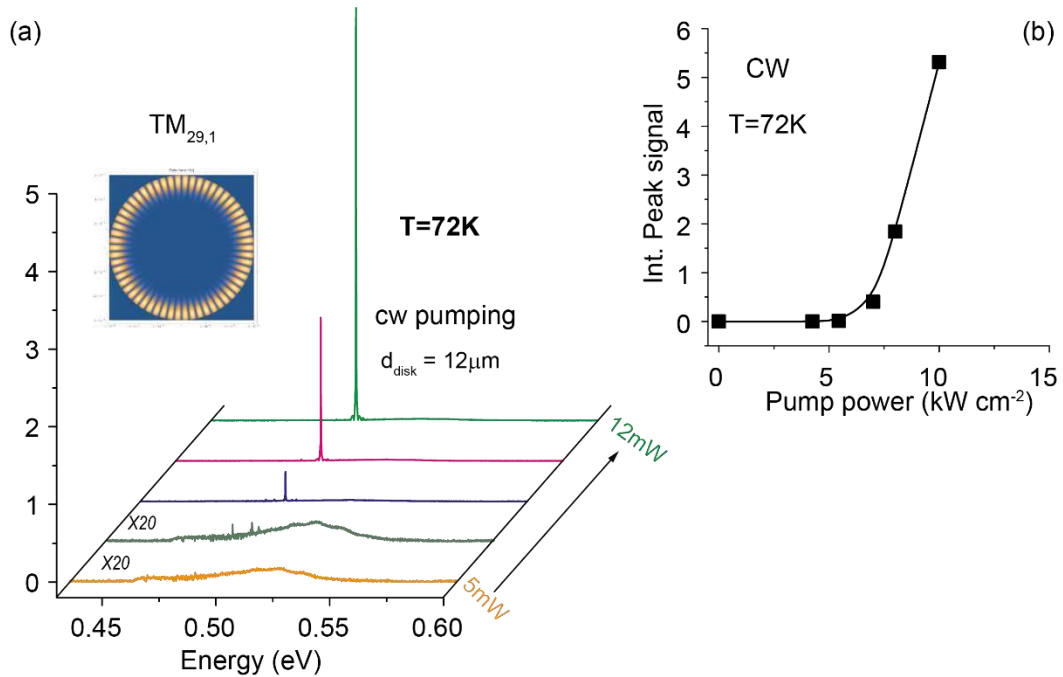


Figure SI-8: (a) The spectra and the (b) L-L curve at 72K for a 12 μm GeSn disk.

7. Modal gain assuming SRH model

To investigate the effect of thermal activation of defects on the modal gain, we perform comparative modeling of gain in two cases, shown in Figure SI-9. The energy difference $\Delta E_{L-\Gamma}$, also called directness, corresponds to the one deduced from the **k.p** modeling of the photoluminescence (70 meV). The valence band splitting ΔE_{LH-HH} amounts to 172 meV. Two cases have been considered: one, where the carrier density is kept constant at 10^{18} cm^{-3} when increasing the temperature, and the second scenario, in which the non-radiative lifetime follows the temperature dependence as given in Ref. [5]. In the first case, the gain decreases with temperature because carriers thermally transfer from Γ to the L valley. In the second case, the injected carrier density decreases with temperature also due to activation of trap levels, following the SRH model of the lifetime, and an activation energy of 19 meV was used, as in Ref. [5]. This results in the modal gain sharply decreasing above 50 K.

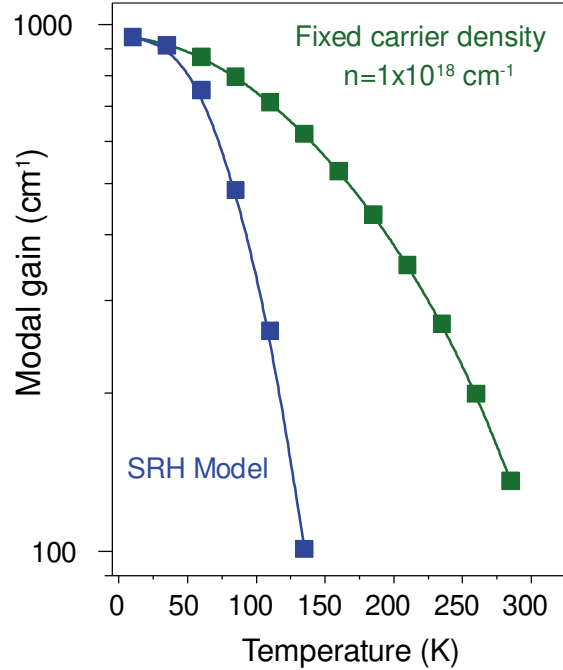


Figure SI-9: Modal gain versus temperature for two scenarios: i) the carrier density is kept constant as temperature varies, and ii) the carrier density decreases due to the SRH-like decrease of the non-radiative recombination time.

8. Steady-state electron distribution in conduction band versus temperature

The steady-state electron distribution was calculated using the band dispersion from the **k.p** model for Γ , and the effective mass based dispersion for L-valley. Figure SI-10a shows the temperature dependence of the equilibrium fraction of electron population in the Γ -valley (the remaining part being in L-valley) for an electron density in the active layer of 10^{18} cm^{-3} (as in Fig. SI-9) for two different biaxial strain values. Larger tensile strain, which increases the $\Delta E_{L-\Gamma}$ difference, is highly beneficial for Γ population, being able to compensate for the larger DOS of the L-valley. This is particularly useful at higher temperatures, where electrons can access higher DOS regions well inside the conduction band. Since only Γ electrons contribute to gain and L-electrons only bring in the free-carrier absorption, the fraction of electrons in Γ should be reasonably large. Clearly, the 1.5% tensile strain in a $\text{Ge}_{0.94}\text{Sn}_{0.06}$ alloy enables larger Γ population, as large as is achievable in relaxed or compressively strained GeSn with much larger Sn content. Increasing biaxial tensile strain to 2%, more challenging technologically, will also enable a $N_{\Gamma}/N_{\text{total}}$ population ratio over 50%, offering higher operation temperature.

While the large Sn content alloys suffer from a large density of defects/non-radiative recombination centers, too large strain may also bring in material quality issues (bulk defects, device operating lifetime). A trade-off between these two approaches needs to be found to enable room temperature lasing. Figure SI-10b shows the temperature dependent electron population fraction in Γ for different Sn contents in 1.5% tensile strained GeSn alloys, which highlights the influence of this parameter on the electron distribution in the Γ -valley. As can be seen for the case of 6 at.% Sn content, with lower $\Delta E_{L-\Gamma}$ splitting, electron population decreases rapidly with increasing temperature, as seen experimentally in the manuscript.

However medium Sn contents of 10 at.% give a larger directness, which allows larger Γ -valley population. This will increase the gain and result in higher operation temperature.

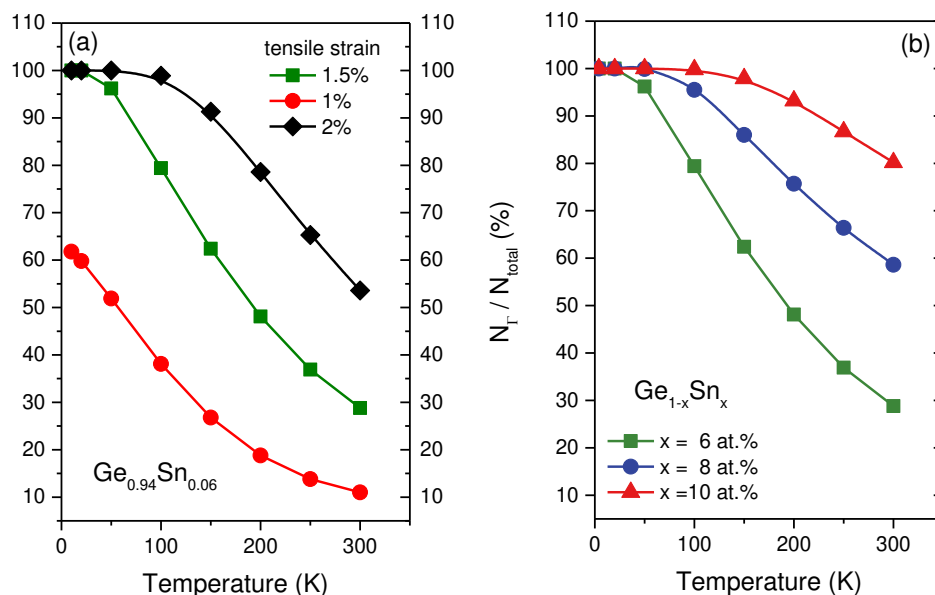


Figure SI-10: (a) Electron fraction in Γ -valley in GeSn alloy with Sn content of 6 at.% under tensile strain of 1%, 1.5% and 2%. (b) Electron fraction in Γ -valley for a tensile strain of 1.5% in GeSn alloys with Sn content of 6 at.%, 8 at.% and 10 at.%.

References

- Hartmann, J.-M., Abbadie, A., Cherkashin, N., Grampeix, H. & Clavelier, L. Epitaxial growth of Ge thick layers on nominal and 6° off Si(001); Ge surface passivation by Si. *Semicond. Sci. Technol.* **24**, 055002, DOI: [10.1088/0268-1242/24/5/055002](https://doi.org/10.1088/0268-1242/24/5/055002) (2009).
- Stange, D. et al. Optically Pumped GeSn Microdisk Lasers on Si. *ACS Photonics* **3**, 1279–1285, DOI: [10.1021/acsphotonics.6b00258](https://doi.org/10.1021/acsphotonics.6b00258) (2016)
- Ghrib, A. et al. Tensile-strained germanium microdisks. *Appl. Phys. Lett.* **102**, 221112, DOI: [10.1063/1.4809832](https://doi.org/10.1063/1.4809832) (2013).
- Elbaz, A. et al. Solving thermal issues in tensile-strained Ge microdisks. *Opt. Express* **26**, 28376–28384, DOI: [10.1364/OE.26.028376](https://doi.org/10.1364/OE.26.028376) (2018).
- Wirths, S. et al. Lasing in direct-bandgap GeSn alloy grown on Si. *Nat. Photonics* **9**, 88–92, DOI: [10.1038/nphoton.2014.321](https://doi.org/10.1038/nphoton.2014.321) (2015)